AIAA JOURNAL
Vol. 48, No. 10, October 2010

Acoustic Analogy Formulations Accelerated by Fast Multipole Method for Two-Dimensional Aeroacoustic Problems

William R. Wolf* and Sanjiva K. Lele†
Stanford University, Stanford, California 94305-4035

DOI: 10.2514/1.J050338

The calculation of acoustic field solutions due to aeroacoustic sources is performed for a large number of observer locations. Sound generation by vortex shedding is computed by a hybrid method and an accurate two-dimensional direct calculation, and the results are compared. The hybrid approach uses direct calculation for near-field source computations and the Ffowcs-Williams–Hawkings equation as the acoustic analogy formulation. The integrations of surface dipole and volume quadrupole source terms appearing in the Ffowcs-Williams–Hawkings formulation are accelerated by a wideband multilevel adaptive fast multipole method. The wideband multilevel adaptive fast multipole method presented here applies a plane-wave expansion formulation for calculations in the high-frequency regime and a partial-wave expansion formulation in the low-frequency regime. The method is described in detail for the solution of a two-dimensional Green's function that incorporates convective effects. The method presented in this work is applied to two-dimensional calculations. However, it can be easily extended to three-dimensional calculations of surface monopole and dipole source terms and volume quadrupole source terms. Results for acoustic field solutions obtained by the accelerated Ffowcs-Williams–Hawkings formulation are 2 orders of magnitude faster when compared with the direct computation of the Ffowcs-Williams–Hawkings equation.

Nomenclature

c	=	speed of sound
D	=	diagonal operator in plane-wave expansion formulation
F_i	=	dipole source
f	=	Ffowcs-Williams–Hawkings surface
G	=	Green's function
H	=	Heaviside function
$H_n^{(2)}$	=	Hankel function of the second kind and order n
I	=	shifting operator in plane-wave expansion formulation
i	=	imaginary unit
J_n	=	Bessel function of the first kind and order n
K	=	modified wave number
k	=	wave number
L_{HF}	=	local expansion for high-frequency regime
L_{LF}	=	local expansion for low-frequency regime
M	=	Mach number
M_{HF}	=	multipole expansion for high-frequency regime
M_{LF}	=	multipole expansion for low-frequency regime
p	=	pressure
Q	=	monopole source
R	=	regular function in partial-wave expansion formulation
S	=	singular function in partial-wave expansion formulation
St	=	Strouhal number
T_{ij}	=	quadrupole source (Lighthill stress tensor)
t	=	time
U_i	=	uniform velocity vector
u_i	=	fluid velocity vector
X_i	=	observer location in transformed coordinates
x_i	=	observer location
Y_i	=	source location in transformed coordinates
y_i	=	source location
δ	=	Dirac delta function
δ_{ij}	=	Kronecker delta
θ	=	polar angle of arbitrary vector
ρ	=	density
τ_{ij}	=	viscous stress tensor
ϕ	=	polar angle of plane wave
ω	=	angular frequency

Subscript

0	=	freestream property

Superscript

$'$	=	acoustic property

Presented as Paper 2009-3231 at the 15th AIAA/CEAS Aeroacoustics Conference, Miami, FL, 11–13 May 2009; received 10 November 2009; revision received 11 February 2010; accepted for publication 09 April 2010.

*Ph.D. Candidate, Department of Aeronautics and Astronautics.

†Professor, Department of Aeronautics and Astronautics, Department of Mechanical Engineering.

I. Introduction

NOISE regulations have become more stringent and, to achieve the required noise reductions, it is important to develop more sophisticated physics-based noise-prediction tools. The design of three-dimensional (3-D) realistic configurations requires the use of time-consuming numerical simulations for the study and mitigation of jet, fan, and airframe noise sources. Direct simulation of noise remains prohibitively expensive for engineering problems because of resolution requirements. Therefore, hybrid approaches that consist of predicting near-field flow quantities by a suitable computational fluid dynamics (CFD) simulation and far-field sound radiation by an acoustic analogy formulation are more attractive. The flow physics associated with sound generation must be accurately captured in the CFD calculation in order to be used in this context.

The Ffowcs-Williams–Hawkings (FW–H) [1] acoustic analogy formulation is used when moving rigid or flexible bodies are present. In this formulation, acoustic pressure fluctuations are predicted by solving an inhomogeneous wave equation with surface monopole and dipole and volume quadrupole source terms. Quadrupole sources are often neglected in sound calculations from low-Mach-number flow simulations, since monopole and dipole sound contributions are dominant. However, for jet flows, they have to be computed, since they are the dominant noise sources and, for wake and shear layer flows, quadrupole sources have an important contribution to noise generation.

For design purposes, it is important to compute acoustic field solutions in order to understand the interaction between noise sources and complex geometries, including scattering and diffraction of sound waves by sharp corners and cavities, for example. Moreover, complete directivity mappings may be required for the study of far-field noise radiated from realistic 3-D configurations. The solution of acoustic analogy formulations for field plots and spherically resolved directivity mappings requiring many observer locations presents a high computational cost. In [2], Lockard discusses a parallel implementation of the FW–H formulation in order to overcome this drawback.

In this paper, a hybrid method is used to study the sound generation by low-Mach-number flows past aerodynamic geometries. To reduce the computational cost of field solutions at many observer locations, the integrations of surface dipole and volume quadrupole source terms are accelerated by a wideband multilevel adaptive fast multipole method (MLFMM) [3]. The wideband MLFMM presented here applies a plane-wave expansion formulation [4,5] for calculations in the high-frequency regime and a partial-wave expansion formulation [5,6] in the low-frequency regime. The method is described in detail for the solution of a two-dimensional (2-D) Green's function that incorporates convective effects [7,8]. Although the method developed in this paper is applied for 2-D dipole and quadrupole integrations, it can be easily extended to accelerate 2-D surface integrations of monopole and dipole source terms, as well as 3-D volume integrations of quadrupole source terms.

To reduce simulation costs, interpolation schemes are applied to obtain noise sources on coarser acoustic grids when CFD grids are overrefined for acoustic simulations [9]. It is shown in [9,10] that these schemes can introduce errors in the results. With the acceleration provided by the method described in this paper, noise sources from CFD grids can be directly used for acoustic predictions. The method can be also applied to obtain scattered field solutions from boundary integral equation methods, such as the boundary element method or the equivalent source method. The study of sound generated by landing gears and high-lift devices can benefit from the method developed here since fast and accurate field solutions can be obtained for complex configurations.

II. Flow Simulation

The general curvilinear form of the compressible Navier–Stokes equations is solved using direct calculation of flows for low Mach and low to moderate Reynolds numbers. This direct calculation resolves the unsteady flow, as well as the acoustic field generated by the flow. The numerical scheme for spatial discretization is a sixth-order-accurate compact scheme [11] implemented on a staggered grid. The current numerical capability allows the use of overset grids with a fourth-order-accurate Hermitian interpolation between grid blocks [12]. The time integration of the fluid equations is carried out by a fully implicit second-order Beam–Warming scheme [13] in the near-wall region in order to overcome the time step restriction. A third-order Runge–Kutta scheme is used for time advancement of the equations in flow regions far away from solid boundaries. No-slip adiabatic wall boundary conditions are applied along the solid surfaces and characteristic plus sponge boundary conditions are applied in the far-field locations. The numerical tool has been previously validated for several compressible flow simulations [12,14].

III. Acoustic Predictions

The FW–H [1] acoustic analogy formulation is used to predict the acoustic field radiated by the unsteady flow simulations. In this work, we present results for 2-D flow simulations; therefore, the acoustic formulation for the 2-D case is shown. Source terms, observer locations, and scattering bodies are assumed to be in steady uniform motion in a stagnant medium. Therefore, following the development of Lockard [7], we apply a Galilean transformation to the FW–H equation. Thus, considering a mean flow in the x Cartesian direction and writing the surface velocity vector $\mathbf{v} = (-U_1, 0)^t$, the FW–H formulation can be written as

$$\left(\frac{\partial}{\partial t} + U_1 \frac{\partial}{\partial x_1}\right)^2 [\rho' H(f)] - c_0^2 \frac{\partial^2 [\rho' H(f)]}{\partial x_j \partial x_j} = \frac{\partial [Q\delta(f)]}{\partial t} - \frac{\partial [F_i \delta(f)]}{\partial x_i} + \frac{\partial^2 [T_{ij} H(f)]}{\partial x_i \partial x_j} \tag{1}$$

where ρ' stands for the acoustic density, c_0 is the speed of sound, and U_1 is the mean flow velocity in the x Cartesian direction ($U_2 = 0$ in the present formulation).

The monopole source term is $Q = [\rho(u_i + U_i) - \rho_0 U_i]\partial f/\partial x_i$, the dipole source term is

$$F_i = [p\delta_{ij} - \tau_{ij} + \rho(u_i - U_i)(u_j + U_j) + \rho_0 U_i U_j]\partial f/\partial x_j$$

and T_{ij} is the Lighthill stress tensor or quadrupole source term given by

$$T_{ij} = \rho u_i u_j + (p' - c_0^2 \rho')\delta_{ij} - \tau_{ij}$$

Here, u_i is the fluid velocity vector, p is the pressure, ρ_0 is the freestream density, p' is the acoustic pressure, δ_{ij} is the Kronecker delta, and τ_{ij} is the viscous stress tensor, for which the effects are considered negligible for the acoustic problems analyzed in the present work. The term f represents the FW–H surface, and $H(f)$ is the Heaviside function, defined as $H(f) = 1$ for $f > 0$ and $H(f) = 0$ for $f < 0$. Applying a Fourier transform to Eq. (1), it can be written in the frequency domain as

$$\left[(1 - M^2)\frac{\partial^2}{\partial x_1^2} + \frac{\partial^2}{\partial x_2^2} + k^2 + i2kM\frac{\partial}{\partial x_1}\right][\hat{p}' H(f)] = -[i\omega \hat{Q}\delta(f)] - \frac{\partial [\hat{F}_i \delta(f)]}{\partial x_i} + \frac{\partial^2 [\hat{T}_{ij} H(f)]}{\partial x_i \partial x_j} \tag{2}$$

where M is the freestream Mach number defined as $M \equiv U_1/c_0$, $\hat{p}'$, $\hat{Q}$, $\hat{F}_i$, and $\hat{T}_{ij}$ are the frequency domain acoustic pressure, monopole, dipole, and Lighthill stress terms, respectively, and k is the wave number. Equation (2) can be rewritten as the Helmholtz equation after a Prandtl–Glauert transformation; then, the Green's function can be obtained, as shown by Lacerda et al. [8], as

$$G(\mathbf{x}, \mathbf{y}) = \frac{i}{4\sqrt{1 - M^2}} e^{iM[k/(1-M^2)](x_1 - y_1)} \times H_0^{(2)}\left[\frac{k}{(1 - M^2)}\sqrt{(x_1 - y_1)^2 + (1 - M^2)(x_2 - y_2)^2}\right] \tag{3}$$

In Eq. (3), $\mathbf{x} = (x_1, x_2)^t$ is an observer location, $\mathbf{y} = (y_1, y_2)^t$ is a source location, and $H_0^{(2)}$ is the Hankel function of the second kind and order zero. In [7], Lockard manipulates Eq. (2) in order to write the following integral equation for the acoustic pressure field solution:

$$[\hat{p}' H(f)] = -\int_{f=0} \left[i\omega \hat{Q}(\mathbf{y}) G(\mathbf{x}, \mathbf{y}) + \hat{F}_i(\mathbf{y}) \frac{\partial G(\mathbf{x}, \mathbf{y})}{\partial y_i}\right] \mathrm{d}S - \int_{f>0} \hat{T}_{ij} H(f) \frac{\partial^2 G(\mathbf{x}, \mathbf{y})}{\partial y_i \partial y_j} \mathrm{d}V \tag{4}$$

In the present work, the surface integrations appearing in Eq. (4) are computed along the scattering body surfaces. Therefore, $u_i = -U_i$ for the monopole and dipole source terms, which are then given by $Q = -\rho_0 U_i \partial f/\partial y_i$ and $F_i = [p\delta_{ij} + \rho_0 U_i U_j]\partial f/\partial y_j$, respectively. Furthermore, one can observe that the monopole source terms, Q, and the second component of the dipole source terms, $\rho_0 U_i U_j$, are steady in time and do not appear in the frequency domain formulation. The volume integrations in Eq. (4) are computed along a subset region of the flowfield, including the wake-plus-boundary-layer regions, where the magnitude of quadrupole sources is nonnegligible. Generally, for low-Mach-number flows, these volume integrals are neglected, since the effects of quadrupole source terms are small when compared with those of dipole and monopole source terms. Furthermore, these calculations are expensive, since large

volume regions have to be integrated in order to avoid the effects of eddies exiting from the source integration domain. Wang et al. [15] show that these escaping eddies generate spurious noise that may contaminate severely the acoustic field solution. They also developed a method to overcome this difficulty. However, for jet flows, quadrupole sources have to be computed, since they are the dominant noise sources and, for wake and shear layer flows, quadrupole sources have an important contribution to noise generation. With the method presented in this work, the computational cost of these volume integrations is considerably reduced.

IV. Multilevel Fast Multipole Method

In this work, the surface and volume integrations of dipole and quadrupole source terms are performed using a wideband MLFMM [3] in order to accelerate the calculations. In the current context, the MLFMM consists of clustering noise source terms at different spatial lengths in multipole expansions and evaluating their effects at clusters of observer locations well separated from noise sources. We define two well-separated clusters as sets of elements (sources and observers) that are circumscribed by circles and for which the centroids are distant from each other by a length of at least four times their radius.

In the fast FW–H method, a CFD grid containing surface and volume noise sources and an acoustic grid containing many observer locations are surrounded by a square box. Then, a recursive algorithm for the refinement of this box is applied in order to form the refinement levels of the MLFMM. The general idea consists of refining the box into four smaller boxes that will be at level 1 and inspecting the number of sources and observers contained by each of the new boxes. This process continues until the number of elements inside all the boxes is smaller than or equal to a certain prescribed number. This prescribed number of elements per box will define the maximum refinement level in the MLFMM. In Fig. 1a, one can observe a refined noise source region surrounding a NACA0012 airfoil and its wake, and in Fig. 1b, the entire computational box is shown surrounding the noise sources in the center of the box and the observer locations in the far field. In the adaptive refinement algorithm, boxes of level $l+1$ are children of the parent boxes of level l. Each parent box is divided into four children, and these are direct neighbors among themselves, which means that they share a common node or edge. Following a quad-tree algorithm, one can write a structure containing all the children from all boxes at all levels. At every level of refinement, a table of nonempty boxes is maintained, so that, once an empty box is encountered, its existence is forgotten, and it is not used in the subsequent process.

To implement the FMM, we define a set of lists containing some specific boxes, such as direct neighbors, parent neighbors, and others. These lists will help with the computation of multipole and local expansions, including their translations and conversions. List L_1 of a box b consists of box b itself and all boxes that do not contain children boxes and share a node or edge with b. If b is a parent box, then $L_1 = 0$. List L_2 of a box b consists of all children of b's parent neighbors that are well separated from b. Boxes on list $L_2(b)$ are in the same level of refinement as b. List $L_3(b)$ is empty if b is a parent box, and it consists of all children of b's neighbors, at any level, which do not share a node or vertex with b. Finally, list L_4 of box b is formed by all boxes c, such that $b \in L_3(c)$. One can observe that all boxes in $L_3(b)$ are at higher levels than b (i.e., are smaller than b), and all boxes in $L_4(b)$ are at lower levels than b (i.e., are larger than b). Beyond that, all boxes in $L_4(b)$ do not have children. The authors suggest the paper from Carrier et al. [16] for a more detailed explanation on the FMM implementation, including the adaptive refinement procedure and the several steps described in the following paragraphs.

The FMM is often applied to integral or summation equations that contain degenerate kernels. The Green's function given by Eq. (3) is the degenerate kernel one wants to expand in a suitable form in order to apply the FMM. Instead of computing the influence of all source terms at $\mathbf{y}$ to all observers at $\mathbf{x}$ directly, one can first modify Eq. (3) and write it as

$$G(\mathbf{X},\mathbf{Y}) = \frac{i}{4\sqrt{1-M^2}} e^{iMK(X_1-Y_1)} H_0^{(2)}\left[K\sqrt{(X_1-Y_1)^2+(X_2-Y_2)^2}\right] \quad (5)$$

where

$$\mathbf{X} = (X_1, X_2)^t = (x_1, \sqrt{1-M^2}x_2)^t$$

,

$$\mathbf{Y} = (Y_1, Y_2)^t = (y_1, \sqrt{1-M^2}y_2)^t$$

and $K = k/(1-M^2)$. Then, one can compute multipole approximations representing the acoustic field of clusters of noise sources at observer locations far away from these clusters. Thus, the first step in the FMM algorithm consists of computing all the multipole expansions around the centroids of all childless boxes. All sources inside these boxes are represented in multipole expansions, which are then summed to form a total multipole representation.

Subsequently, all the multipole expansions from the childless boxes at all levels are shifted to the centroids of their parent boxes up to level 2 in the adaptive refinement algorithm. Thus, we have multipole expansions for the boxes in level 2, representing their influence on the field outside each one of these boxes. The translation of multipoles from centroids of boxes of level $l+1$ to their parent centroids at level l will be referred to as $M2M$ translation. Next, the multipole expansions for the boxes in $L_2(b)$ are converted to local expansions about b's centroid and added up, forming a local expansion around b's centroid, representing the acoustic field of the sources from the well-separated boxes at the same level of b. These conversions from multipoles to local expansions around centroids of well-separated boxes will be called $M2L$ conversions. All the local representations from L_2 are then shifted to b's children until the highest refinement level is reached. These translations will be called $L2L$.

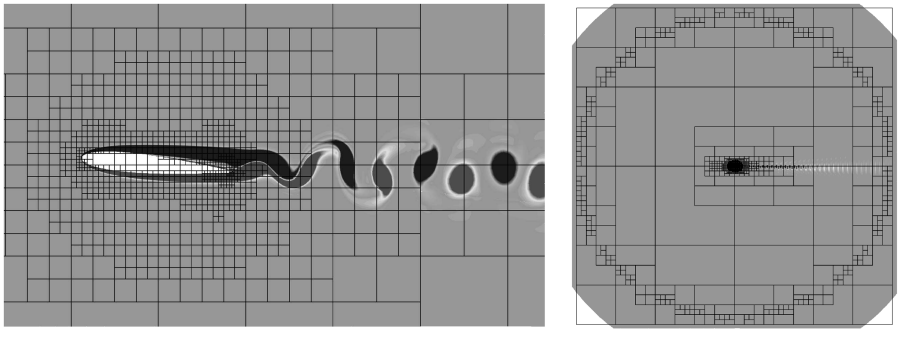

a) Detail of refined source region **b) Refined computational box**

Fig. 1 Adaptive refinement on regions containing acoustic sources and observer locations.

Finally, the local expansions computed for the centroids of the boxes in the highest levels of refinement are used to compute the effects of far-field sources to each of the observer locations contained inside these boxes. Once the effects of the far sources are considered, a further step includes the evaluation of the effects of nearby sources. For each childless box b, we compute the direct interactions among all elements inside b and the elements contained on $L_1(b)$, $L_3(b)$, and $L_4(b)$. All these interactions are calculated using the direct solution of the FW–H equation. Since stability is maintained for any range of frequencies, the wideband MLFMM allows the use of several levels of adaptive refinement in order to have few sources and observer locations inside the childless boxes. Therefore, the computational cost from direct computations is reduced.

The wideband MLFMM described in this paper uses a partial-wave expansion formulation for computations in the low-frequency regime and a plane-wave expansion formulation in the high-frequency regime. The reason for using these two different formulations is that the former is stable for all frequency ranges but has a higher computational cost when compared with the latter. Therefore, it is expensive to use at high frequencies. The latter has a lower computational cost but is unstable at low frequencies. Using the partial-wave expansion method [5,6], the Green's function from Eq. (5) can be written as

$$G(\mathbf{X},\mathbf{Y}) = \frac{i}{4\sqrt{1-M^2}} e^{iMK(X_1-Y_1)} \sum_{n=-\infty}^{\infty} S^n(\mathbf{oX}) R^{-n}(\mathbf{oY}) \tag{6}$$

where the singular S^n and regular R^n functions are defined as $S^n(\mathbf{w}) = i^n H_n^{(2)}(Kr)e^{in\theta}$ and $R^n(\mathbf{w}) = (-i)^n J_n(Kr)e^{in\theta}$. In these expressions, $H_n^{(2)}$ and J_n stand for the nth-order Hankel function of the second kind and the Bessel function of the first kind, respectively. The terms r and θ are the polar coordinates of some vector $\mathbf{w}$, which can be $\mathbf{oX}$ or $\mathbf{oY}$, for instance. The vectors $\mathbf{oX}$ and $\mathbf{oY}$ point from some box center, $\mathbf{o}$, to a far away observer location, $\mathbf{X}$, and a nearby source location, $\mathbf{Y}$, respectively. Using the plane-wave expansion method [4,5], the Green's function from Eq. (5) can be written as

$$G(\mathbf{X},\mathbf{Y}) = \frac{i}{8\pi\sqrt{1-M^2}} e^{iMK(X_1-Y_1)} \times \oint I(\mathbf{oY},\mathbf{K}) D(\mathbf{oo}',\mathbf{K}) I(\mathbf{o}'\mathbf{X},\mathbf{K})\, \mathrm{d}(\mathbf{K}/|\mathbf{K}|) \tag{7}$$

where the shifting operator is given by $I(\mathbf{oY},\mathbf{K}) = e^{-i\mathbf{K}\cdot\mathbf{oY}}$, and the diagonal translation operator is given by

$$D(\mathbf{oo}',\mathbf{K}) = \sum_{n=-\infty}^{\infty} e^{-in\phi} i^n H_n^{(2)}(K|\mathbf{oo}'|) e^{in\theta}$$

In these expressions, $\mathbf{o}$ is a box center close to the source location at $\mathbf{Y}$, $\mathbf{o}'$ is a box center close to observer location at $\mathbf{X}$, θ is the polar angle of vector $\mathbf{oo}'$, and ϕ is the polar angle of a plane-wave sample $\mathbf{K}$. In both formulations, the number of terms used in the functions S, R, and D, and the number of plane-wave samples along the unit circle, have to be truncated. The number of truncation terms and plane-wave samples depends on the refinement level and is given by the formula $\varphi_{lv} = \lfloor ka_{lv} + c\log(ka_{lv}+\pi)\rfloor$ [17], where $\lfloor\cdot\rfloor$ stands for the integer part, a_{lv} is the box size at refinement level lv, and the constant c controls the desired accuracy of the solution. This constant is chosen as $c = 8$ in the present calculations in order to provide high accuracy in the FMM calculations. The choice of a particular value for c depends on the accuracy desired in the FMM calculations. The authors suggest the papers from Darve [18] and Song and Chew [19] for details regarding the accuracy of the method and the choice of constant c. The number of plane-wave samples per refinement level is $2\varphi_{lv}$.

Since each method is used for distinct frequency ranges, the subscripts LF and HF will be introduced to operations performed by the partial-wave expansion method in the low-frequency range and the plane-wave expansion method in the high-frequency range, respectively. Applying the LF and HF formulations to the FW–H equation, one can write multipole expansions as

$$\begin{aligned} M_{\mathrm{LF}} = M_n(\mathbf{o}) = &\int_{f=0} \Bigg[i\omega\hat{Q} R^n(\mathbf{oY}) e^{-iMKY_1} \\ &+ \hat{F}_i \frac{\partial[R^n(\mathbf{oY})e^{-iMKY_1}]}{\partial Y_l} \frac{\partial Y_l}{\partial y_i} \Bigg] \mathrm{d}S \\ &+ \int_{f>0} \hat{T}_{ij} \frac{\partial^2[R^n(\mathbf{oY})e^{-iMKY_1}]}{\partial Y_l \partial Y_m} \frac{\partial Y_l}{\partial y_j} \frac{\partial Y_m}{\partial y_i}\, \mathrm{d}V \end{aligned} \tag{8}$$

and

$$\begin{aligned} M_{\mathrm{HF}} = M(\mathbf{o},\mathbf{K}) = &\int_{f=0} i\omega\hat{Q} I(\mathbf{oY},\mathbf{K}) e^{-iMKY_1} \\ &+ \hat{F}_i \frac{\partial[I(\mathbf{oY},\mathbf{K})e^{-iMKY_1}]}{\partial Y_l} \frac{\partial Y_l}{\partial y_i}\, \mathrm{d}S \\ &+ \int_{f>0} \hat{T}_{ij} \frac{\partial^2[I(\mathbf{oY},\mathbf{K})e^{-iMKY_1}]}{\partial Y_l \partial Y_m} \frac{\partial Y_l}{\partial y_j} \frac{\partial Y_m}{\partial y_i}\, \mathrm{d}V \end{aligned} \tag{9}$$

In the expressions above, $\mathbf{o}$ is a box center close to the source location at $\mathbf{Y}$. Equations (8) and (9) should be used to compute multipole expansions for small childless boxes in the low-frequency regime M_{LF} and large childless boxes in the high-frequency regime M_{HF}, respectively. However, computations using Eq. (8) are more expensive due to the multiple computations of Bessel functions and Bessel-function derivatives. Therefore, one can reduce the computational cost if all multipole expansions are calculated through Eq. (9), which only requires calculations with exponentials and derivatives of exponentials. Then, multipole expansions M_{HF} can be transformed to M_{LF} through the Jacobi–Anger identity, as shown by Rokhlin [4], and a backward fast Fourier transform (b-FFT) can be used to accelerate the computations. The steps described above can be observed in the wideband MLFMM diagram shown in Fig. 2.

For the partial-wave expansion formulation, the $M2M_{\mathrm{LF}}$ operations are given by

$$M_n(\mathbf{o}') = \sum_{v=-\varphi_{lv+1}}^{\varphi_{lv+1}} R^{n-v}(\mathbf{o}'\mathbf{o}) M_v(\mathbf{o}); \qquad n = -\varphi_{lv},\ \ldots,\ \varphi_{lv} \tag{10}$$

In Eq. (10), $\mathbf{o}'$ is the center of a parent box, and $\mathbf{o}$ is the center of one of its children. To avoid computations of the $R^{n-v}(\mathbf{o}'\mathbf{o})$ functions for all boxes at all levels, these functions are computed and stored in a previous step. Since the distances $\mathbf{o}'\mathbf{o}$ are the same inside each level of refinement, we have to save a small number of function values that require negligible memory storage. In the plane-wave expansion method, $M2M_{\mathrm{HF}}$ operations are performed by plane waves represented along the unit circle. The plane-wave directions $\mathbf{K}$ are given by the polar angles ϕ, and for each refinement level lv, the number of wave samples is increased when the translation occurs from a higher level to a lower level. Therefore, interpolation of multipole expansions is performed along the circle perimeter. Since the M_{HF} multipole representation along the unit circle is periodic, we use a Fourier interpolation formulation that can be implemented with a FFT as

$$\begin{aligned} f^n &= \frac{1}{J}\sum_{j=1}^{J} M[\mathbf{o},\mathbf{K}(\phi_j^{lv+1})] e^{-in\phi_j^{lv+1}} \\ M[\mathbf{o},\mathbf{K}(\phi_j^{lv})] &= \sum_{n=-N}^{N} f^n e^{in\phi_j^{lv}} \end{aligned} \tag{11}$$

Once interpolation is performed, the multipole expansions are shifted from the centroids of the children boxes $\mathbf{o}$ to the centroids of the parent boxes $\mathbf{o}'$ as

$$M[\mathbf{o}',\mathbf{K}(\phi_j^{lv})] = e^{i\mathbf{K}\cdot\mathbf{oo}'} M[\mathbf{o},\mathbf{K}(\phi_j^{lv})] \tag{12}$$

In the wideband MLFMM, $M2M_{\mathrm{LF}}$ operations are performed for small boxes at high levels of refinement, and $M2M_{\mathrm{HF}}$ operations are performed for large boxes at low levels of refinement. During the translations from higher to lower levels of refinement, the local Helmholtz numbers increase, and the high-frequency regime formulation can be applied. Therefore, the multipole expansions M_{LF} are converted to M_{HF} through a Jacobi–Anger expansion [4]. A forward fast Fourier transform (f-FFT) accelerates these calculations, as shown in the wideband MLFMM diagram from Fig. 2.

In the low-frequency regime, $M2L_{\mathrm{LF}}$ conversions are performed by

$$L_n(\mathbf{o}') = \sum_{\nu=-\varphi_{lv}}^{\varphi_{lv}} S^{n-\nu}(\mathbf{oo}')M_\nu(\mathbf{o}); \qquad n = -\varphi_{lv}, \ \ldots, \ \varphi_{lv} \tag{13}$$

and in the high-frequency regime, $M2L_{\mathrm{HF}}$ conversions are performed by

$$L(\mathbf{o}', \mathbf{K}) = D(\mathbf{oo}', \mathbf{K})M(\mathbf{o}, \mathbf{K}) \tag{14}$$

In these expressions, $\mathbf{o}'$ is the center of a box b, containing the observer location $\mathbf{X}$, and $\mathbf{o}$ is the center of a box in $L_2(b)$. This is the most expensive step in the MLFMM, since many $M2L$ conversions are computed for all boxes at all levels. The computational costs for the $M2L_{\mathrm{LF}}$ and $M2L_{\mathrm{HF}}$ operations are $O(\varphi_{lv}^2)$ and $O(\varphi_{lv})$, respectively. Therefore, $M2L_{\mathrm{HF}}$ conversions should be used whenever possible. However, computations performed using this formulation become unstable for higher levels of refinement with small local Helmholtz numbers. This problem is referred in the literature as subwavelength breakdown, and the authors refer to the works from Nishimura [5] and Dembart and Yip [20] for a detailed discussion on the topic. To overcome this drawback, the low-frequency formulation is applied to the high levels of refinement with small local Helmholtz numbers. The cost for these computations is small, since this formulation is used only for high levels of refinement, where the number of truncations terms φ_{lv} is small. Furthermore, the values of $S^{n-\nu}(\mathbf{o}'\mathbf{o})$ can be previously stored for all the $\mathbf{o}'\mathbf{o}$ combinations at high levels of refinement, reducing the computational cost of this step. Similarly, values of $D(\mathbf{oo}', \mathbf{K})$ are also stored for all combinations of $\mathbf{oo}'$ at low levels of refinement. The boundary between the low-frequency and high-frequency regimes is defined by the desired accuracy of the method. In the present work, following the results presented in [3], the low-frequency formulation is applied when the local box size a_{lv} becomes $a_{lv} < 3.5\lambda$, where λ is the acoustic wavelength.

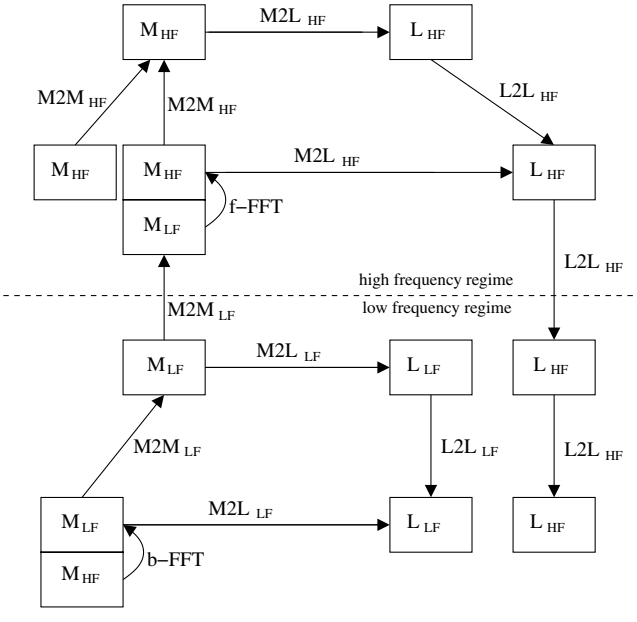

Fig. 2 Schematic diagram for the wideband MLFMM algorithm.

Differently from $M2M_{\mathrm{HF}}$, in the wideband MLFMM, $L2L_{\mathrm{HF}}$ operations are performed for boxes at all levels of refinement, from lower levels to finer levels. However, $L2L_{\mathrm{LF}}$ operations are performed only for small boxes at high levels of refinement, as shown in the wideband MLFMM diagram from Fig. 2. In the wideband FMM from [3], local representations L are converted from L_{HF} to L_{LF}, and for high levels of refinement, only conversions $L2L_{\mathrm{LF}}$ are used. In the present work, these conversions are not performed, since they require computational effort. Furthermore, $L2L_{\mathrm{HF}}$ presents the same computational complexity as $L2L_{\mathrm{LF}}$.

For the partial-wave expansion formulation, the $L2L_{\mathrm{LF}}$ operations are given by

$$L_n(\mathbf{o}') = \sum_{\nu=-\varphi_{lv-1}}^{\varphi_{lv-1}} R^{n-\nu}(\mathbf{o}'\mathbf{o})L_\nu(\mathbf{o}); \qquad n = -\varphi_{lv}, \ \ldots, \ \varphi_{lv} \tag{15}$$

In Eq. (15), $\mathbf{o}'$ is the center of a child box, and $\mathbf{o}$ is the center of its parent. The values for the $R^{n-\nu}(\mathbf{o}'\mathbf{o})$ functions were stored for $M2M_{\mathrm{LF}}$. In the plane-wave expansion method, $L2L_{\mathrm{HF}}$ operations are performed by plane waves represented along the unit circle. The number of wave samples decreases when the translation occurs from a lower level to a higher level of refinement. Therefore, filtering of local expansions are performed along the circle perimeter. Before filtering is performed, the local expansions L_{HF} are shifted from the centroids of the parent boxes $\mathbf{o}$ to the centroids of the children boxes $\mathbf{o}'$,

$$L[\mathbf{o}', \mathbf{K}(\phi_j^{lv-1})] = e^{i\mathbf{K}\cdot\mathbf{oo}'}L(\mathbf{o}, \mathbf{K}[\phi_j^{lv-1})] \tag{16}$$

Then, since the local representations along the unit circle are periodic, we use a Fourier filtering formulation that can be implemented with a FFT as

$$f^n = \frac{1}{J}\sum_{j=1}^{J} L[\mathbf{o}', \mathbf{K}(\phi_j^{lv-1})]e^{-in\phi_j^{lv-1}}$$

$$L[\mathbf{o}', \mathbf{K}(\phi_j^{lv})] = \frac{1}{2}\sum_{n=-N}^{N} f^n e^{in\phi_j^{lv}} \tag{17}$$

Calculations of acoustic pressure can finally be performed by

$$\begin{aligned}[\hat{p}'H(f)] = {} & \left\{ -\int_{f=0}\left[i\omega\hat{Q}(\mathbf{y})G(\mathbf{x}, \mathbf{y}) + \hat{F}_i(\mathbf{y})\frac{\partial G(\mathbf{x}, \mathbf{y})}{\partial y_i}\right] \mathrm{d}S \right. \\ & \left. - \int_{f>0} \hat{T}_{ij}H(f)\frac{\partial^2 G(\mathbf{x}, \mathbf{y})}{\partial y_i \partial y_j}\,\mathrm{d}V \right\}_{\mathrm{FW\text{-}H}} \\ & + \left\{ \frac{i}{4\pi\sqrt{1-M^2}}\left[\frac{1}{2\pi}\oint e^{i\mathbf{K}\cdot\mathbf{oX}}e^{iMKX_1}L(\mathbf{o}, \mathbf{K})\,\mathrm{d}(\mathbf{K}/|\mathbf{K}|) \right.\right. \\ & \left.\left. + \sum_{n=-\varphi_{lv}}^{\varphi_{lv}} (-1)^n e^{iMKX_1}I^n(\mathbf{oX})L_{-n}(\mathbf{o}) \right] \right\}_{\mathrm{MLFMM}} \end{aligned} \tag{18}$$

where the terms with subscript FW–H represent nearby calculations among sources and observer locations, and those with subscript MLFMM represent distant calculations. The integral in Eq. (18) is discretized by a trapezoidal integration with weights ω_s and plane-wave samples uniformly spaced along the unit circle perimeter as

$$\begin{aligned}[\hat{p}'H(f)] = {} & \left\{ -\int_{f=0}\left[i\omega\hat{Q}(\mathbf{y})G(\mathbf{x}, \mathbf{y}) + \hat{F}_i(\mathbf{y})\frac{\partial G(\mathbf{x}, \mathbf{y})}{\partial y_i}\right] \mathrm{d}S \right. \\ & \left. - \int_{f>0} \hat{T}_{ij}H(f)\frac{\partial^2 G(\mathbf{x}, \mathbf{y})}{\partial y_i \partial y_j}\,\mathrm{d}V \right\}_{\mathrm{FW\text{-}H}} \\ & + \left\{ \frac{i}{4\pi\sqrt{1-M^2}}\left[\frac{1}{2\pi}\sum_{s=1}^{S} \omega_s e^{i\mathbf{K}\cdot\mathbf{oX}}e^{iMKX_1}L(\mathbf{o}, \mathbf{K}) \right.\right. \\ & \left.\left. + \sum_{n=-\varphi_{lv}}^{\varphi_{lv}} (-1)^n e^{iMKX_1}I^n(\mathbf{oX})L_{-n}(\mathbf{o}) \right] \right\}_{\mathrm{MLFMM}} \end{aligned} \tag{19}$$

V. Results

This section discusses results obtained by direct calculation and the fast FW–H formulation. A study of sound generated by low-speed flows past a cylinder, a NACA0012 airfoil, and the combination of both is performed together with an assessment in terms of computational cost of the fast FW–H and conventional FW–H formulations. The solutions are shown in terms of directivity and field plots, and the effects of convection and quadrupole source integrations are assessed. A grid-refinement study is performed in order to assure that solutions are converged, and only results obtained for the most refined grids are discussed. The acoustic simulations are performed by a computer with a 1.66 GHz Intel Core 2 Duo T5450 CPU and 2 Gb RAM. The direct calculations obtained by the flow solver are performed by a cluster computer with 2.33 GHz Intel Xeon CPUs.

A. Cylinder Vortex Shedding

Sound generated by an unsteady laminar flow past a cylinder is studied as the first problem. The flow Reynolds number based on the cylinder diameter is $Re = 180$, and the Mach number is $M = 0.3$. Results for similar computational simulations can be found in the literature in the papers from Inoue and Hatakeyma [21], Gloerfelt et al. [22], and Sharma and Lele [23] for a range of Reynolds and Mach numbers comparable to that considered in the present work.

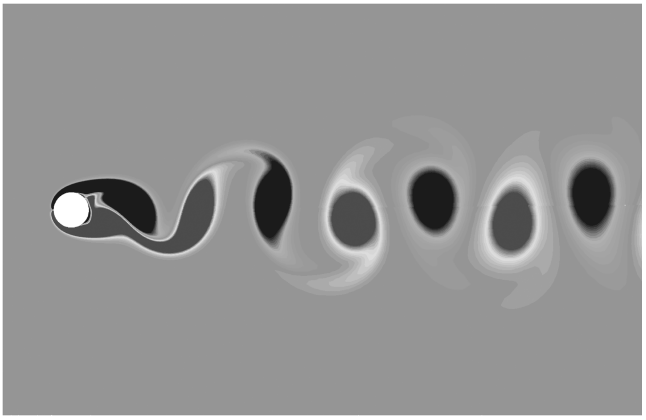

Fig. 3 Vorticity field for $Re = 180$ and $M = 0.3$ around the cylinder region.

The radiated sound field is available from a direct calculation and is compared with that from a hybrid method (unsteady simulation plus FW–H). For the direct calculation obtained by the flow solver, an O mesh with 360×600 grid points is used. The spacing between the first grid point and the cylinder wall in the radial direction is 0.001, and the grid stretching factor is 1.015. The grid spacing in the polar direction is uniform. The far-field location is at $280R$, where R is the radius of the cylinder. The total cost of the direct calculation obtained by the flow solver is ≈700 CPU hours for this simulation. The high cost of the direct calculation is due to the need to accurately capture the unsteady flow in the sound-generation region and also the sound propagation to the observer location in the far field. The cost of the sound propagation is eliminated in a hybrid method. One can observe a plot of the vorticity flowfield around the cylinder region in Fig. 3. The Strouhal numbers obtained for the vortex-shedding frequency and the second-harmonic frequency are $St = f2R/U = 0.19$ and $St = 0.38$, respectively. The solutions obtained by the hybrid method include the integration of surface dipole and volume quadrupole source terms. The quadrupole terms are integrated along the cylinder and wake regions, and one can see a detail plot of their intensities for the vortex-shedding and second-harmonic frequencies in Fig. 4a–4f, respectively. It is observed that, for the former frequency, the intensity of $\hat{T}_{12}$ shows a slower decay along the wake region when compared with $\hat{T}_{11}$ and $\hat{T}_{22}$ and, for the latter frequency, both $\hat{T}_{12}$ and $\hat{T}_{22}$ present a slower decay along the wake when compared with $\hat{T}_{11}$.

In Fig. 5a, one can see a directivity plot for the vortex-shedding frequency for observer locations at $220R$, which corresponds to ≈6 acoustic wavelengths. Results are presented for the direct calculation and fast FW–H solution with dipole source terms (see Table 1 for comparison of computational cost), and one can observe the expected lift dipole directivity and the effects of convection for the vortex-shedding frequency. The solution obtained by the fast FW–H formulation, including convection effects, shows excellent agreement with that obtained by direct calculation. However, the solution with no convection effects underpredicts acoustic pressure. Effects of quadrupole source terms are negligible for this particular frequency. In Fig. 5b, one can see the directivity plot for the second-harmonic frequency for observer locations at $160R$, which corresponds to ≈9 acoustic wavelengths. A drag dipole directivity is observed for this frequency and, as expected, its intensity is one order of magnitude smaller than that for the lift dipole. In the figure, one can observe a comparison of the solutions obtained by the fast FW–H formulation and the direct calculation. In the solution represented by open circles, convection effects and quadrupole source terms are neglected. One can observe that this solution underpredicts upstream acoustic

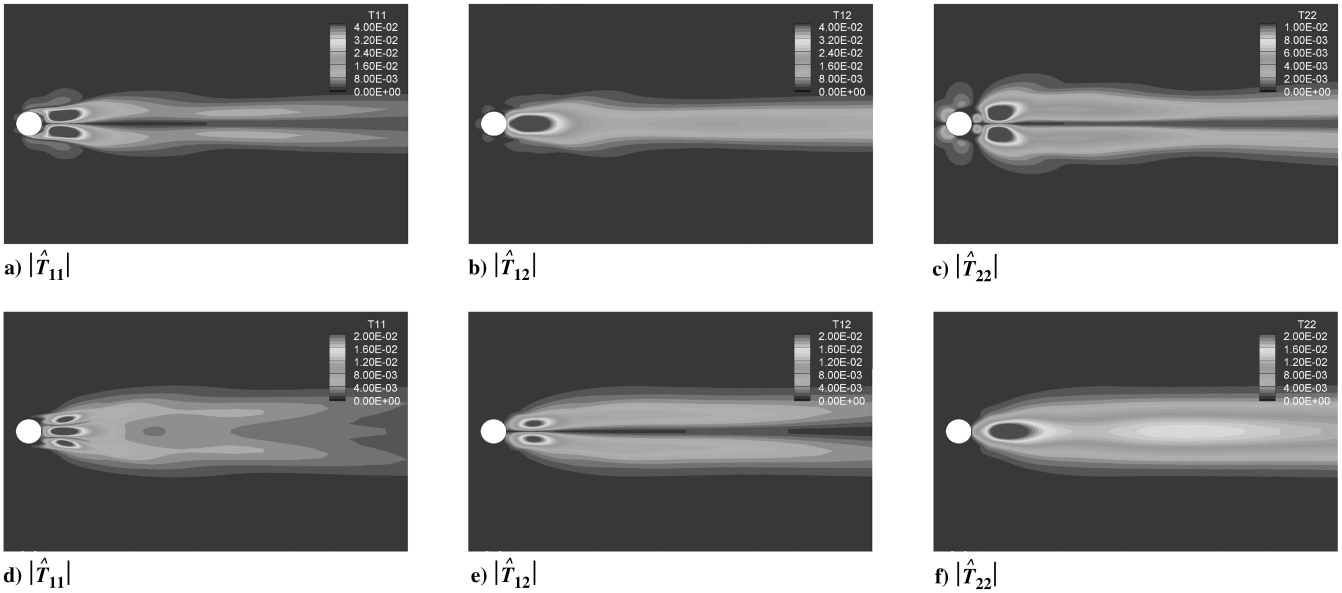

a) $|\hat{T}_{11}|$ b) $|\hat{T}_{12}|$ c) $|\hat{T}_{22}|$

d) $|\hat{T}_{11}|$ e) $|\hat{T}_{12}|$ f) $|\hat{T}_{22}|$

Fig. 4 Magnitude of quadrupole source terms for a–c) the vortex-shedding frequency and d–f) the second-harmonic frequency.

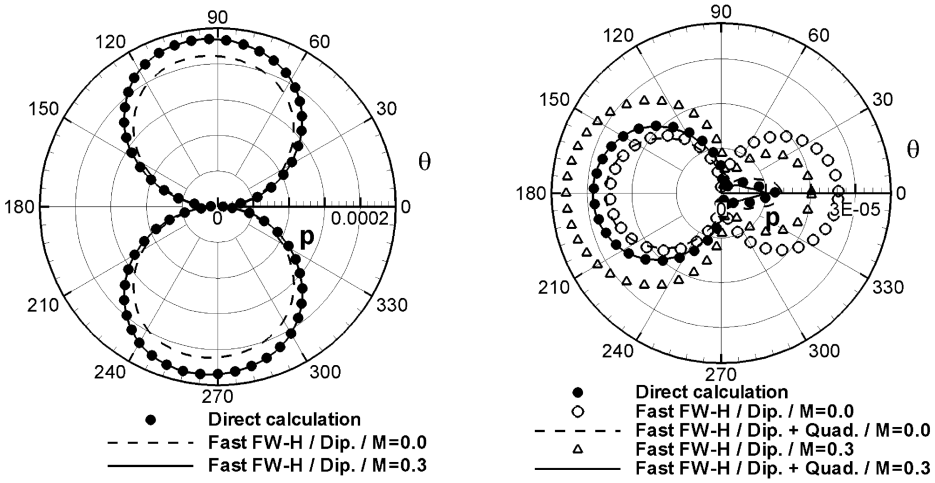

a) Vortex shedding frequency b) Second harmonic frequency

Fig. 5 Directivity plots for observer locations at a) 220*R* and b) 160*R* distant from the cylinder.

pressure and overpredicts downstream acoustic pressure. For the dashed line solution, convection effects are neglected but quadrupole source terms are included. One can see that upstream acoustic pressure is still underpredicted; however, downstream acoustic pressure shows a better agreement with direct calculation. When convection effects are included and quadrupole source terms are neglected, both upstream and downstream acoustic pressures are overpredicted. In the solution represented by the continuous line, both convection effects and quadrupole source terms are included, and one can observe the excellent agreement between the hybrid method and direct calculation. For this particular frequency, the effects of quadrupole source terms are more evident than that of convection.

The directivity plots in Figs. 5a and 5b are obtained for 360 observer locations by the fast FW–H formulation in 3.7*s* and 4.2*s*, respectively. The computational time for directivity plots obtained through the conventional solution of the FW–H formulation is 116.6*s*. Therefore, factors of 31.5 and 27.7 in computational cost reduction are observed.

Figure 6 shows acoustic field solutions for the first- and second-harmonic frequencies obtained by the fast FW–H formulation. The accelerated integrals are computed over the cylinder and wake regions, containing 81,000 quadrupole sources from the direct calculation mesh and two acoustic grids with 90×70 grid points. For these acoustic grids, the number of points per wavelength in the radial direction is ≈ 8. The maximum number of source terms per box is set equal to 2000, and the maximum number of observer locations is set equal to five for the acoustic mesh used in the solution shown in Figs. 6a and 7 for that used in the solution shown in Fig. 6b. With these parameters, determined by numerical experimentation, 13 levels of adaptive refinement are used for both the vortex-shedding frequency and for the second-harmonic frequency simulations. The computational time for the conventional solution of the FW–H formulation is 2834.3*s*, while those for the fast FW–H solutions are 13.0*s* for the vortex-shedding frequency, implying a factor of 218.0 in computational cost reduction and 14.3*s* for the second-harmonic frequency, implying a factor of 198.2 in computational cost reduction. In Tables 2 and 3, one can see summaries in terms of computational cost for field plots for the conventional solution of the FW–H formulation and for the fast FW–H solution.

Table 1 Computational cost (in seconds) for directivity plots and cost-reduction factor

	Cyl. 1st harm.	Cyl. 2nd harm.	NACA0012	NACA0012 + Cyl.
Directivity plot FW–H	116.6	116.6	258.3	310.2
Directivity plot MLFMM	3.7	4.2	12.9	27.9
Cost-reduction factor	31.5	27.7	20.0	11.1

B. NACA0012

In the second problem, we consider the sound generated by the flow past a NACA0012 airfoil, with a rounded trailing edge at an angle of attack of $\alpha = 5$ deg.. The flow Reynolds number based on the airfoil chord is $Re = 5000$, and the Mach number is $M = 0.3$. The papers of Wang et al. [15] and Nagarajan and Lele [24] present results of computational simulations for a similar range of Reynolds and Mach numbers. Sound generation is computed by direct calculation, and a hybrid method and results for the vortex-shedding frequency are compared. For the direct calculation, an *O* grid with 400×620 grid points is used, and the far-field location is at $25c$, where c is the airfoil chord. The spacing between the first grid point and the airfoil wall in the radial direction is 0.0005, and the grid stretching factor is 1.01. A stretching of grid points along the airfoil direction is used in order to cluster points in the leading and trailing edges. In the leading edge, the minimum grid spacing along the airfoil direction is 0.005 and, in the trailing edge, it is 0.0005. The total cost of the direct calculation obtained by the flow solver is ≈ 800 CPU hours for this simulation. Again, the high cost of the direct calculation is due to the need to accurately capture the unsteady flow in the sound-generation region and also the sound propagation to the observer location in the far field. The vorticity field around the airfoil region is shown in Fig. 7. The Strouhal number obtained for the vortex-shedding frequency is $St = fc/U = 1.83$, where $U = 0.3$ is the nondimensional velocity, and $f = 0.55$ is the nondimensional frequency. The solution obtained by the hybrid method includes the integration of surface dipole and volume quadrupole source terms. The quadrupole terms are integrated along the airfoil and wake regions, and a detail plot of their intensities is shown for the vortex-shedding frequency in Fig. 8. One can observe that the intensity of $\hat{T}_{22}$ is one order of magnitude weaker than $\hat{T}_{11}$ and $\hat{T}_{12}$.

In Fig. 9, one can see a directivity plot for the vortex-shedding frequency for 360 observer locations at $17c$, which corresponds to ≈ 9 acoustic wavelengths. Results are presented for the conventional calculation and fast FW–H formulation, neglecting (Fig. 9a) and including (Fig. 9b) convective effects and the integration of quadrupole source terms.

In the solution represented by open circles in Fig. 9a, convective effects and quadrupole source terms are neglected. In the same figure, the dashed–dotted-line solution neglects convective effects but includes quadrupole integrations. For the dashed line solution in Fig. 9b, convective effects are included and quadrupole source terms are neglected, and for the continuous line solution, both convective effects and quadrupole source elements are included. One can

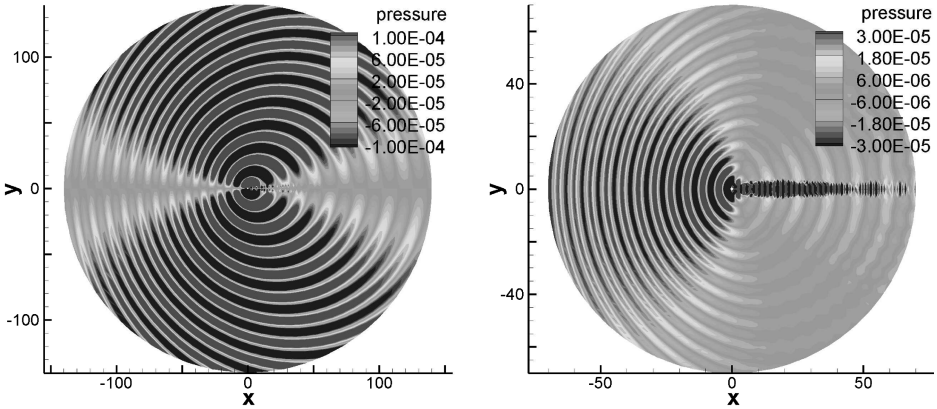

a) Vortex shedding frequency **b) Second harmonic frequency**

Fig. 6 Acoustic fields obtained by the fast FW–H formulation.

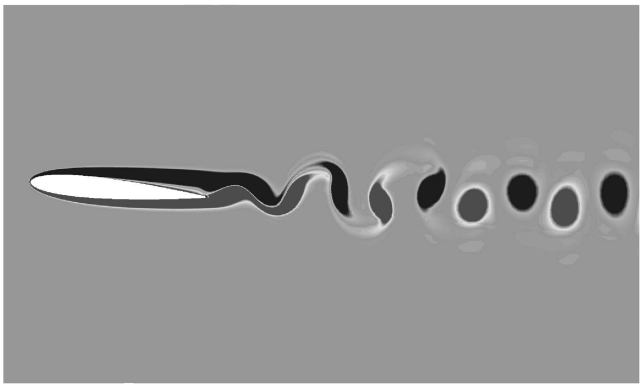

Fig. 7 Vorticity field for $Re = 5000$ and $M = 0.3$ around the NACA 0012 airfoil region.

observe that both solutions without convective effects underpredict acoustic pressure. The dashed-line solution shows a better agreement of acoustic pressure when compared with the direct calculation. However, this solution slightly underpredicts peak values of acoustic pressure and does not capture the downstream lobes appearing in the direct calculation. When convective effects and quadrupole source terms are included the solution obtained by the hybrid method shows excellent agreement with the direct calculation, as can be observed in the continuous-line solution. The directivity plot in Fig. 9 is obtained by the fast FW–H formulation in 12.9s. The computational time for a directivity plot obtained through the conventional solution of the FW–H formulation is 258.3s. Therefore, a factor of 20.0 in computational cost reduction is observed. These results can be observed in a comparison of computational cost presented in Table 1.

Figures 10a and 10b show acoustic field solutions for the vortex-shedding frequency obtained by the direct calculation and the fast FW–H formulation, respectively. The results are in excellent agreement. However, one can observe slight differences in the nonlinear wake region. One can also notice the damping of acoustic waves in the far-field region of the direct calculation due to the sponge layer. The accelerated integrals are computed over a wake region containing 168,000 quadrupole sources and an acoustic field with 180×190 grid points. The maximum number of source elements per box is set equal to 5000, and the maximum number of observer locations is set equal to 10 for the acoustic mesh. With these parameters, 14 levels of adaptive refinement are used. The computational time for the conventional solution of the FW–H formulation is 20915.0s, while that for the fast FW–H solutions is 47.8s, implying a factor of 437.5 in computational cost reduction. One can see summaries in terms of computational cost for field plots in Tables 2 and 3.

Table 2 Computational cost (in seconds) for field plots, neglecting volume quadrupole integrations and cost-reduction factor

	Cyl. 1st harm.	Cyl. 2nd harm.	NACA0012	NACA0012 + Cyl.
Dipole field FW–H	36.8	36.8	150.7	175.8
Dipole field MLFMM	3.6	4.7	11.7	14.9
Cost-reduction factor	10.2	7.8	12.8	11.7

Table 3 Computational cost (in seconds) for field plots, including volume quadrupole integrations and cost-reduction factor

	Cyl. 1st harm.	Cyl. 2nd harm.	NACA0012	NACA0012 + Cyl.
Total field FW–H	2834.3	2834.3	20915.0	25661.8
Total field MLFMM	13.0	14.3	47.8	114.0
Cost-reduction factor	218.0	198.2	437.5	225.1

C. NACA0012 Plus Cylinder

In the last problem, sound generated by the unsteady flow past a NACA0012 airfoil with a rounded trailing edge and a cylinder located close to its trailing-edge boundary-layer region is studied. The configuration is at an angle of attack of $\alpha = 5$ deg. The Reynolds number based on the airfoil chord is $Re = 5000$, and the Reynolds number based on the diameter of the cylinder is $Re = 200$. The Mach number is $M = 0.3$. In the paper of Singer et al. [25], a similar configuration composed by airfoil plus a bluff-body vortex generator is studied. However, that study addressed the scattering of vortices generated by artificial viscosity past the bluff body and convected through the sharp trailing edge. In this study, the scattering of sound generated by the cylinder wake on the cylinder and airfoil surfaces is analyzed. Sound generation is computed by direct calculation, and a hybrid method and results for the vortex-shedding frequency are compared. For the direct calculation, two overset O grids are used along the boundary-layer regions of the NACA0012 and cylinder, and a background O grid is used to capture the wake regions and acoustic field. The NACA0012 boundary-layer grid has 400×60 grid points, the cylinder boundary-layer grid has 240×45 grid points, and the background grid has 400×625 grid points, and the far-field location is at $25c$, where c is the airfoil chord. The background grid used in this simulation is similar to that used in the previous test case. The total cost of the direct calculation obtained by the flow solver is $\approx$1500 CPU hours for this simulation. The vorticity field around the airfoil and cylinder region is shown in Fig. 11. The Strouhal number obtained for the vortex-shedding frequency is $St = fc/U = 4.43$, based on the chord length, and $St = f2R/U = 0.19$, based on the cylinder diameter. Here, the nondimensional velocity is $U = 0.3$, and the nondimensional frequency is $f = 1.33$. The solution obtained by the hybrid method includes the integration

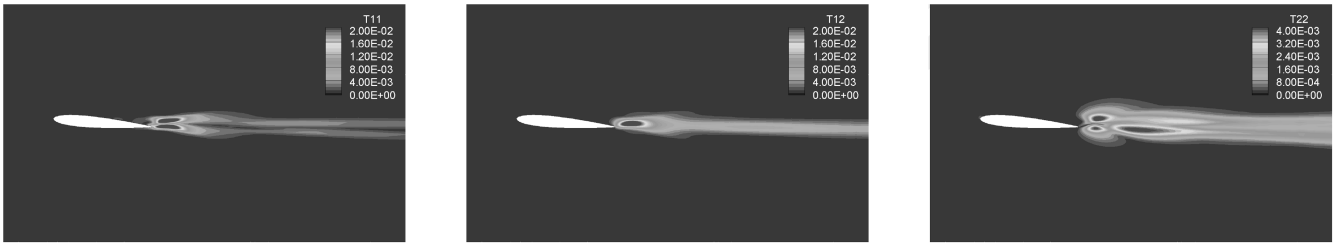

a) $|\hat{T}_{11}|$ b) $|\hat{T}_{12}|$ c) $|\hat{T}_{22}|$

Fig. 8 Magnitude of quadrupole source terms for the vortex-shedding frequency.

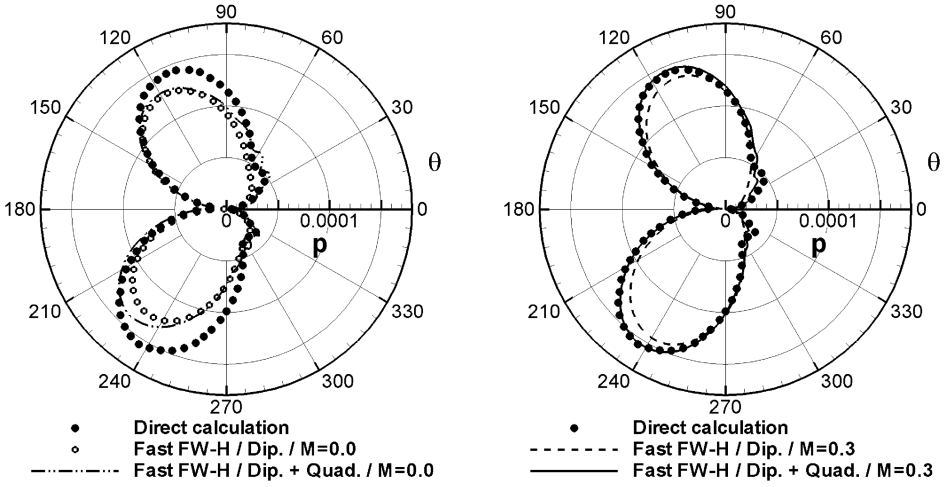

a) Neglecting convection effects b) Including convection effects

Fig. 9 Directivity plot for the vortex-shedding frequency for an observer location at 17*c* distant from the NACA0012 airfoil.

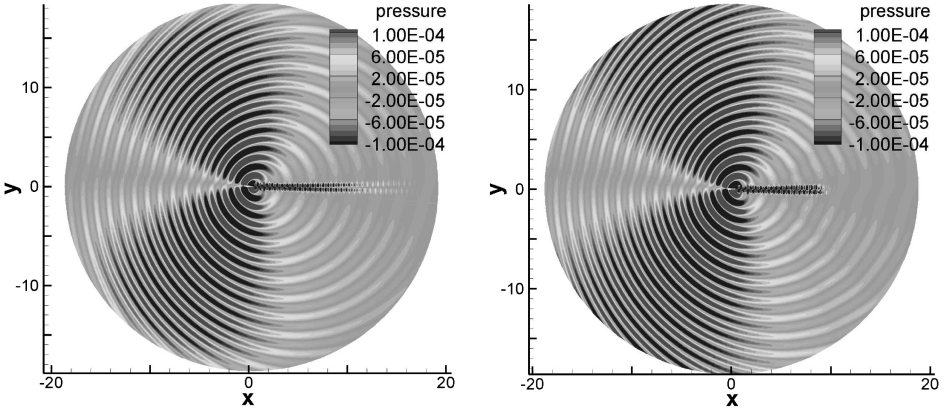

a) Direct calculation b) Fast FW-H formulation

Fig. 10 Acoustic field for the vortex-shedding frequency.

Fig. 11 Vorticity field around the NACA0012 airfoil and cylinder regions.

of surface dipole and volume quadrupole source terms. The quadrupole terms are integrated along the airfoil, cylinder, and wake regions, and a detail plot of their intensities is shown for the vortex-shedding frequency in Fig. 12. One can see that their intensities have a fast decay along the wake region, and that the magnitude of quadrupole sources along the airfoil wake region is almost negligible when compared with that from the cylinder wake.

In Fig. 13, one can see a directivity plot for the vortex-shedding frequency for an observer location at 6*c*, which corresponds to $\approx$8 acoustic wavelengths. Results are presented for the direct calculation and fast FW–H formulation, and the effects of convection and quadrupole integrations are shown. As one can observe in the results obtained by direct calculation, this configuration shows a complex directivity pattern for the vortex-shedding frequency. Sound is radiated toward the top region of the airfoil, due to scattering along the cylinder and airfoil surfaces. Radiation in the upstream and

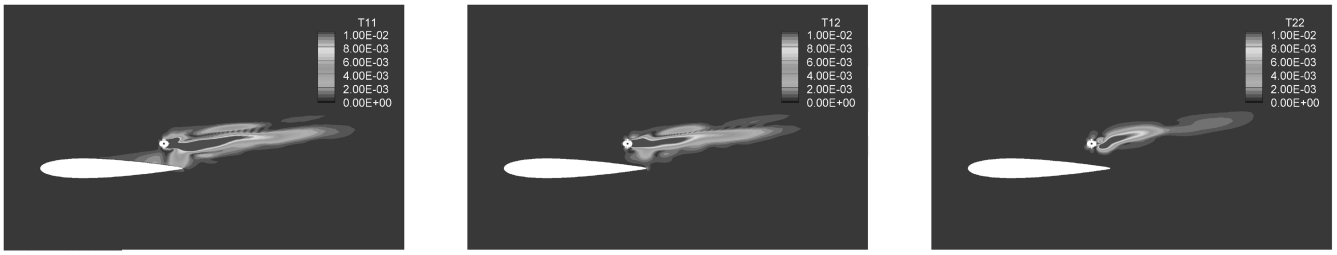

a) $|\hat{T}_{11}|$ b) $|\hat{T}_{12}|$ c) $|\hat{T}_{22}|$

Fig. 12 Magnitude of quadrupole source terms for the vortex-shedding frequency.

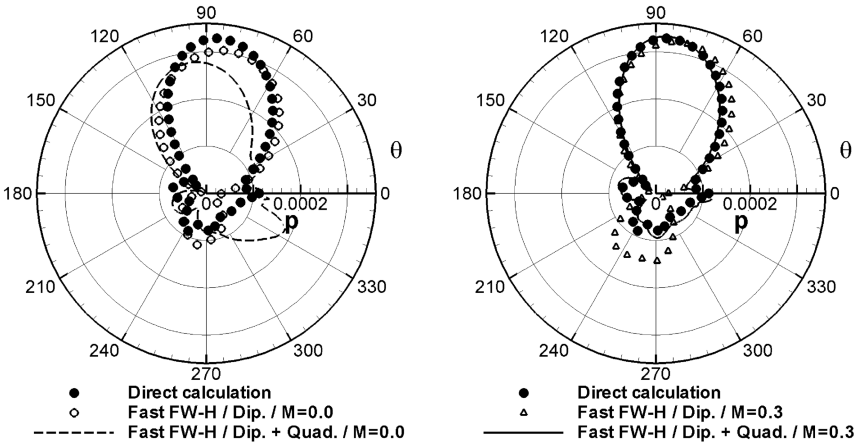

a) Neglecting convection effects b) Including convection effects

Fig. 13 Directivity plot for the vortex-shedding frequency for an observer location at 6*c* distant from the NACA0012 airfoil.

downstream directions is due solely to quadrupole sources, and sound radiated in the region below the airfoil occurs from the combination of diffraction along the airfoil and radiation due to quadrupole sources. In the solutions presented in Fig. 13a, convective effects are neglected. The full symbols represent the direct calculation solution, the open symbols represent the fast FW–H solution without quadrupoles, and the dashed-line solution includes quadrupoles. One can observe that the solution represented by open circles is more scattered than the direct calculation solution, underpredicts the peak values of acoustic pressure along the top region of the airfoil, and overpredicts acoustic pressure below it. Also, neither of the upstream and downstream lobes are captured. The dashed-line solution shows a poor agreement with the direct calculation solution at all angles. Figure 13b presents results, including convection effects. Again, full symbols represent the direct calculation, the open symbols represent the fast FW–H solution without quadrupoles, and the full-line solution includes quadrupole effects. One can observe that, although the solution represented by open triangles shows a reasonable agreement with the direct calculation in terms of magnitude of acoustic pressure along the top region of the airfoil, it is slightly shifted. Furthermore, acoustic pressure is overpredicted along the bottom region, and the upstream and downstream lobes are not captured. When convective effects and quadrupole source terms are included, the solution obtained by the hybrid method shows good agreement with the direct calculation, as can be observed in the continuous-line solution. Directivity of acoustic pressure is well represented along the top region of the airfoil, and the upstream and downstream lobes are captured. The bottom region shows a slight difference between the direct calculation and the fast FW–H solutions. The directivity plots in Figs. 13a and 13b are obtained by the fast FW–H formulation in 27.9*s*. The computational time for a directivity plot obtained through the conventional solution of the FW–H formulation is 310.2*s*. Therefore, a factor of 11.1 in computational cost reduction is observed. These

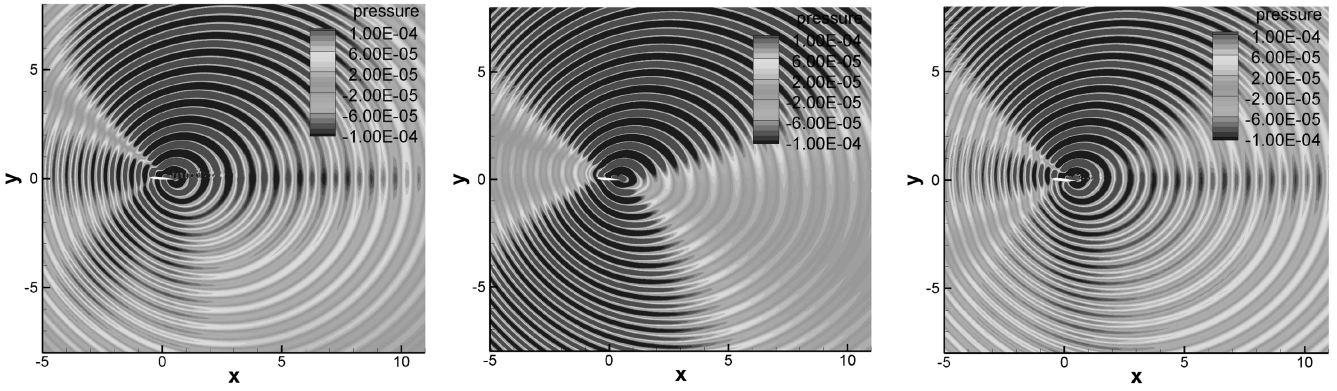

a) Direct calculation b) Fast FW-H formulation: dipoles c) Fast FW-H formulation: dipoles + quadrupoles

Fig. 14 Acoustic field for the vortex-shedding frequency.

results can be observed in a comparison of computational cost presented in Table 1.

Figures 14a–14c show acoustic field solutions for the vortex-shedding frequency obtained by the direct calculation and the fast FW–H formulation, neglecting and including quadrupole integrations, respectively. The results between the direct calculation and fast FW–H solution with quadrupoles are in good agreement. However, one can observe slight differences in the cylinder nonlinear wake region and in the bottom region of the airfoil. These small differences are already shown in the directivity plots. The solution presented in Fig. 14b shows large differences when compared with the direct calculation and fast FW–H solutions with quadrupoles. The accelerated integrals are computed over a wake region containing 214,000 quadrupole source volume elements and an acoustic field with 180×180 grid points. The maximum number of source elements per box is set equal to 1000, and the maximum number of observer locations is set equal to 30 for the acoustic mesh. With these parameters, 15 levels of adaptive refinement are used. The computational time for the conventional solution of the FW–H formulation is $25,661.8s$, while that for the fast FW–H solutions is $114.0s$, implying a factor of 225.1 in computational cost reduction. One can see summaries in terms of computational cost for field plots in Tables 2 and 3.

VI. Conclusions

The present work concerns the study of sound generated by aerodynamic flows for low Mach and low to moderate Reynolds numbers. Solutions obtained by a hybrid method that computes noise source terms using direct calculation and applies the FW–H acoustic analogy formulation to obtain sound radiation are compared with direct calculation results. All source terms appearing in the FW–H equation are computed, and the surface dipole and volume quadrupole integrations are accelerated by a wideband MLFMM. The method is described in detail for the solution of a 2-D Green's function that incorporates convective effects. Although the wideband MLFMM formulation is used here for 2-D dipole and quadrupole integrations, it can be easily extended to accelerate 2-D surface integrations of monopole and dipole source terms, as well as 3-D volume integrations of quadrupole source terms.

The test cases analyzed in this work include the flow past a cylinder for $Re = 180$ and $M = 0.3$, the flow over a NACA0012 airfoil for $Re = 5000$ and $M = 0.3$, and the flow past both configurations together at $Re = 5000$ and $M = 0.3$. Pressure directivity and acoustic field plots obtained by the fast FW–H formulation are compared with those obtained by direct calculation, and they are in excellent agreement. This paper reports two main contributions: the study of convection effects and quadrupole sources on the acoustic fields of the cases analyzed and the application of a wideband MLFMM to accelerate acoustic analogy formulations for field solutions at many observer locations. Solutions obtained by the fast FW–H formulation show a computational cost reduction of two orders of magnitude. The study of sound generation by flows past complex configurations, such as landing gears and high-lift devices, where wakes and shear layers have important contributions to noise generation, can benefit from the method presented here.

Acknowledgments

The authors acknowledge the support of Fulbright and Coordenação de Aperfeiçoamento de Pessoal de Nível Superior through a Ph.D. Scholarship for the first author, under the Fulbright/CAPES grant no. 2464055. The first author also acknowledges Rathakrishnan Bhaskaran for his comments and suggestions on the use of the overset large-eddy simulation code.

References

[1] Ffowcs Williams, J. E., and Hawkings, D. L., "Sound Generation by Turbulence and Surface in Arbitrary Motion," *Philosophical Transactions of the Royal Society of London, Series A: Mathematical and Physical Sciences*, Vol. 264, No. 1151, 1969, pp. 321–342. doi:10.1098/rsta.1969.0031

[2] Lockard, D. P., "A Comparison of Ffowcs Williams-Hawkings Solvers for Airframe Noise Applications," 8th AIAA/CEAS Aeroacoustics Conference, AIAA Paper 2002-2580, 2002.

[3] Cheng, H., Crutchfield, W. Y., Gimbutas, Z., Greengard, L., Ethridge, J. F., Huang, J., Rokhlin, V., Yarvin, N., and Zhao, J., "A Wideband Fast Multipole Method for the Helmholtz Equation in Three Dimensions," *Journal of Computational Physics*, Vol. 216, No. 1, 2006, pp. 300–325. doi:10.1016/j.jcp.2005.12.001

[4] Rokhlin, V., "Rapid Solution of Integral Equations of Scattering Theory in Two Dimensions," *Journal of Computational Physics*, Vol. 86, No. 2, 1990, pp. 414–439. doi:10.1016/0021-9991(90)90107-C

[5] Nishimura, N., "Fast Multipole Accelerated Boundary Integral Equation Methods," *Applied Mechanics Reviews*, Vol. 55, No. 4, 2002, pp. 299–324. doi:10.1115/1.1482087

[6] Wolf, W. R., and Lele, S. K., "Fast Multipole Boundary Element Method for Sound Scattering from Aerodynamic Bodies," 14th AIAA/CEAS Aeroacoustics Conference, AIAA Paper 2008-2872, 2008.

[7] Lockard, D. P., "An Efficient, Two-Dimensional Implementation of the Ffowcs Williams and Hawkings Equation," *Journal of Sound and Vibration*, Vol. 229, No. 4, 2000, pp. 879–911. doi:10.1006/jsvi.1999.2525

[8] Lacerda, L. A., Wrobel, L. C., and Mansur, W. J., "A Boundary Integral Formulation for Two-Dimensional Acoustic Radiation in a Subsonic Uniform Flow," *Journal of the Acoustical Society of America*, Vol. 100, No. 1, 1996, pp. 98–107. doi:10.1121/1.415871

[9] Wiart, C. C., Georges, L., Geuzaine, P., Detand, Y., and Caro, S., "Analysis of the Noise Source Interpolation Within a Hybrid CAA Method: Application to the Case of the Helmholtz Resonator," 15th AIAA/CEAS Aeroacoustics Conference, AIAA Paper 2009-3115, 2009.

[10] Cristophe, J., Anthoine, J., and Moreau, S., "Trailing Edge Noise of a Controlled-Diffusion Airfoil at Moderate and High Angle of Attack," 15th AIAA/CEAS Aeroacoustics Conference, AIAA Paper 2009-3196, 2009.

[11] Nagarajan, S., Lele, S. K., and Ferziger, J. H., "A Robust High-Order Method for Large Eddy Simulation," *Journal of Computational Physics*, Vol. 191, No. 2, 2003, pp. 392–419. doi:10.1016/S0021-9991(03)00322-X

[12] Bhaskaran, R., and Lele, S. K., "Development of Large Eddy Simulation for Aero-Thermal Prediction in High Pressure Turbine Cascade," 38th AIAA Fluid Dynamics Conference, AIAA Paper 2008-4146, 2008.

[13] Beam, R. M., and Warming, R. F., "An Implicit Factored Scheme for the Compressible Navier–Stokes Equations," *AIAA Journal*, Vol. 16, No. 4, 1978, pp. 393–402. doi:10.2514/3.60901

[14] Nagarajan, S., "Leading Edge Effects in Bypass Transition," Ph.D. Thesis, Stanford Univ., Stanford, CA, 2004.

[15] Wang, M., Lele, S. K., and Moin, P., "Computation of Quadrupole Noise Using Acoustic Analogy," *AIAA Journal*, Vol. 34, No. 11, 1996, pp. 2247–2254. doi:10.2514/3.13387

[16] Carrier, J., Greengard, L., and Rokhlin, V., "A Fast Adaptive Multipole Algorithm for Particle Simulations," *SIAM Journal on Scientific and Statistical Computing*, Vol. 9, No. 4, 1988, pp. 669–686. doi:10.1137/0909044

[17] Coifman, R., Rokhlin, V., and Wandzura, S., "The Fast Multipole Method for the Wave Equation: A Pedestrian Prescription," *IEEE Antennas and Propagation Magazine*, Vol. 35, No. 3, 1993, pp. 7–12. doi:10.1109/74.250128

[18] Darve, E., "The Fast Multipole Method I: Error Analysis and Asymptotic Complexity," *SIAM Journal on Numerical Analysis*, Vol. 38, No. 1, 2000, pp. 98–128. doi:10.1137/S0036142999330379

[19] Song, J. M., and Chew, W. C., "Error Analysis for the Truncation of Multipole Expansion of Vector Green's Functions," *IEEE Microwave and Wireless Components Letters*, Vol. 11, No. 7, 2001, pp. 311–313. doi:10.1109/7260.933781

[20] Dembart, B., and Yip, E., "The Accuracy of Fast Multipole Methods for Maxwell's Equations," *IEEE Computational Science and Engineering*, Vol. 5, No. 3, 1998, pp. 48–56. doi:10.1109/99.714593

[21] Inoue, O., and Hatakeyama, N., "Sound Generation by a Two-Dimensional Circular Cylinder in a Uniform Flow," *Journal of Fluid Mechanics*, Vol. 471, 2002, pp. 285–314.doi:10.1017/S002211 2002002124

[22] Gloerfelt, X., Pérot, F., Bailly, C., and Juvé, D., "Flow-Induced Cylinder Noise Formulated as a Diffraction Problem for Low Mach Numbers," *Journal of Sound and Vibration*, Vol. 287, Nos. 1–2, 2005, pp. 129–151. doi:10.1016/j.jsv.2004.10.047

[23] Sharma, A., and Lele, S. K., "Sound Generation Due to Transient Motion of a Bluff Body: Direct Computation and Acoustic Analogy Predictions," 46th AIAA Aerospace Sciences Meeting and Exhibit, AIAA Paper 2008-0032, 2008.

[24] Nagarajan, S., and Lele, S. K., "Sound Generation by Unsteady Airfoil Motions: A Study Using Direct Computation and Acoustic Analogy," 11th AIAA/CEAS Aeroacoustics Conference, AIAA Paper 2005-2915, 2005.

[25] Singer, B. A., Brentner, K. S., and Lockard, D. P., "Simulation of Acoustic Scattering from a Trailing Edge," *Journal of Sound and Vibration*, Vol. 230, No. 3, 2000, pp. 541–560. doi:10.1006/jsvi.1999.2628

C. Bailly
Associate Editor